

SCIENTIFIC REPORTS



OPEN

Application of Quantitative Microstructural MR Imaging with Atlas-based Analysis for the Spinal Cord in Cervical Spondylotic Myelopathy

Masaaki Hori¹, Akifumi Hagiwara^{1,2}, Issei Fukunaga¹, Ryo Ueda³, Kouhei Kamiya², Yuichi Suzuki², Wei Liu⁴, Katsutoshi Murata⁵, Tomohiro Takamura¹, Nozomi Hamasaki¹, Ryusuke Irie^{1,2}, Koji Kamagata¹, Kanako Kunishima Kumamaru¹, Michimasa Suzuki¹ & Shigeki Aoki¹

Mapping of MR fiber g-ratio, which is the ratio of the diameter of the axon to the diameter of the neuronal fiber, is introduced in this article. We investigated the MR fiber g-ratio, the axon volume fraction (AVF) and the myelin volume fraction (MVF) to evaluate microstructural changes in the spinal cord in patients with cervical spondylotic myelopathy (CSM) *in vivo*, using atlas-based analysis. We used diffusion MRI data acquired with a new simultaneous multi-slice accelerated readout-segmented echo planar imaging sequence for diffusion analysis for AVF calculation and magnetization transfer saturation imaging for MVF calculation. The AVFs of fasciculus gracilis in the affected side spinal cord, fasciculus cuneatus and lateral corticospinal tracts (LSCT) in the affected and unaffected side spinal cord were significantly lower ($P = 0.019, 0.001, 0.0019, 0.000, \text{ and } 0.002$, respectively) than those of normal controls. No difference was found in the MVFs. The fiber g-ratio of LSCT was significantly lower ($P = 0.040$) in the affected side spinal cords than in the normal controls. The pathological microstructural changes in the spinal cord in patients with CSM, presumably partial axonal degenerations with preserved myelin. This technique has the potential to be a clinical biomarker in patients with CSM *in vivo*.

Cervical spondylotic myelopathy (CSM) is a common spinal cord disorder, especially affecting upper middle-aged people¹. Disk degeneration, osteophytic changes, and hypertrophy of ligaments result in stenosis of spinal canal, leading to cervical cord myelopathy. The usefulness of conventional MR imaging, including T1- or T2-weighted imaging, is limited to identification of morphological or relative signal changes, providing only non-specific evaluation of the spinal cord. Further, recent advances in neuroprotective approaches^{2,3} may merit early detection of subclinical damage due to CSM, which cannot be detected on conventional MRI. Thus, quantitative MR imaging analysis for assessing spinal cord damage due to CSM needs to be established. In the past, diffusion MRI (dMRI)⁴⁻⁷, MR spectroscopy⁸ and other advanced MR techniques and their combinations⁹ have been applied to investigate the spinal cords of patients with CSM, revealing abnormalities in areas with compression. These techniques showed potential to improve the diagnosis and management of various spinal pathologies. However, dMRI is vulnerable to susceptibility artifacts, which is known to be exaggerated in stenosed spinal canal, potentially providing inaccurate metrics¹⁰. Further, compression of the spinal cord increase the density of neuronal fibers in the spinal cord, which would increase FA¹¹. Thus, abnormal quantitative values may or may not be reversible after therapy. Recently, Grabher *et al.*¹² showed disrupted DTI metrics in the spinal cords of patients with CSM above the level of stenosis. They also revealed correlation of these metrics with clinical disability, suggesting that

¹Department of Radiology, Juntendo University School of Medicine, Tokyo, Japan. ²Department of Radiology, Graduate School of Medicine, The University of Tokyo, Tokyo, Japan. ³Health Science, Tokyo Metropolitan University, Tokyo, Japan. ⁴Siemens Shenzhen Magnetic Resonance Ltd, Shenzhen, China. ⁵Siemens healthcare Japan, Tokyo, Japan. Correspondence and requests for materials should be addressed to M.H. (email: mahori@juntendo.ac.jp)

	CSM patients (n = 20)	Healthy controls (n = 5)	z/X ²	P
Male/female	9/11	3/2	0.361	0.65
Age (years)	61.1 ± 15.4	45.0 ± 16.1	-1.836	0.71
Affected side				
Left affected	11	0	—	—
Right affected	2	0	—	—
Bilateral affected	7	0	—	—

Table 1. Demographic characteristics of the participants. Values are mean ± SD or n. X² analysis was used to examine sex and the Mann–Whitney U-test was used to examine age.

quantitative MRI in the spinal cord above the level of stenosis could provide unbiased readouts of microstructural damage due to CSM.

Recently, MR fiber g-ratio (the ratio of the diameter of the axon to the diameter of the neuronal fiber) mapping was introduced^{13–15}, and it is expected to be a promising tool in the quantitative measurement of the microstructure of neural tissue *in vivo*¹⁶. Changes in the g-ratio with age and with development in infants have been shown in the literature^{17,18}. These reports concern brain tissue, but there is also a report of MR g-ratio mapping *in vivo* in the spinal cord, in which axon density, calculated from the restricted water fraction of dMRI data, and myelin density were measured *in vivo* with high precision and therefore can be used to create a g-ratio-weighted map¹⁹.

For MR fiber g-ratio mapping, two quantitative MR measurements, the myelin volume fraction (MVF) and the axon volume fraction (AVF), are used to calculate the aggregate g-ratio in a voxel. Several methods of the MVF calculation for quantitative estimation of myelin content have been proposed, such as those based on macromolecular tissue volume²⁰, quantitative magnetization transfer (qMT)²¹, magnetization transfer saturation (MTsat)²² and relaxometry^{23,24}. For AVF calculation to quantitatively estimate axon volumes, diffusion tensor imaging²⁵, q-space imaging^{26,27} and neuronal tissue model-based diffusion analysis, such as neurite orientation dispersion and density imaging (NODDI)^{28–30} have been used. These imaging techniques are used for quantitative MR imaging of myelin and axons; therefore, in addition to the g-ratio itself, the myelin and axon structures can be used separately to report the microstructural condition of a spinal cord *in vivo* using these techniques. Moreover, recent developments of the spinal cord atlas with a probabilistic atlas of the spinal cord, e.g., the dorsal column, are available as a part of the Spinal Cord Toolbox (SCT)³¹. Spinal cord analysis based on SCT showed high reproducibility^{32,33} and is expected to describe each anatomic structure in the spinal cord³⁴ more precisely than the past arbitrary region-of-interest-based studies.

In this work, we investigate the MR fiber g-ratio, the AVF and the MVF as tools to evaluate microstructural changes in the spinal cord above the level of stenosis in patients with CSM *in vivo* using atlas-based analysis.

Results

Data from a total of twenty patients and 5 healthy controls were initially included in this study, and data of 4 patients were excluded because their images suffered unexpected artifacts and seemed to be inappropriate for further analysis. Thus, a total of 20 patients with 26 affected sides and 14 unaffected sides and 5 healthy controls with 10 normal sides were analyzed. The demographic and clinical characteristics of the 20 patients and 5 healthy controls are shown in Table 1. The AVF, the MVF and the MR fiber g-ratio values of bilateral DCs and LCSTs are summarized in Table 2. The AVFs of the fasciculus gracilis in the affected side spinal cord and the fasciculus cuneatus and LSCT in the affected and unaffected side spinal cords were significantly lower ($P = 0.019$, 0.001 , 0.019 , 0.000 , and 0.002 , respectively) than those of the normal controls.

No difference was found in the MVFs. The fiber g-ratio of the LSCT was significantly lower ($P = 0.040$) in the affected side spinal cords than in the normal controls. A representative case is illustrated in Fig. 1. There was no correlation among mJOA scores, number of levels of compression and the above quantitative MR metrics.

Discussion

There is very little literature about the g-ratio of normal spinal cord white matter. Duval *et al.* has recently reported that the mean MR g-ratio of a normal spinal cord white matter was 0.76 ¹⁹, and past histological studies showed that the normal range of g-ratios in central nervous system was $0.6–0.81$ ¹⁹. The results of this study showed that the g-ratio values in normal spinal cord white matter were $0.69–0.74$, which seem to be reasonable. The normal g-ratio values in our study were lower than that reported by Duval *et al.*¹⁹, but within the range reported in previous histological studies. The difference can be partly explained by the difference in MRI acquisition sequences for the MVF and the AVF and the calibration methods for MVF estimation.

Our study showed no significant differences in the MVF among 3 groups of spinal cords. A past pathological study showed that there were thin myelinated fibers, indicating focal demyelination and remyelination, in the damaged white matter at the compressed segment³⁵. Myelin loss or myelin pallor was not observed in the spinal cords of CSM model rat, even though the disease duration was limited to 25 weeks³⁶. In our study, we measured the MVF at the C3 vertebral level, which was above the compressed segment, thus demyelination may not have expanded into the C3 level spinal cord. Another possible explanation is that the MVF may have remained at approximately normal values due to remyelination.

Our results showed that the AVF of the affected side was lower than that of normal controls in all three tracts, with corresponding decrease of g-ratio in LCST. A study of post mortem human spinal cords has suggested that

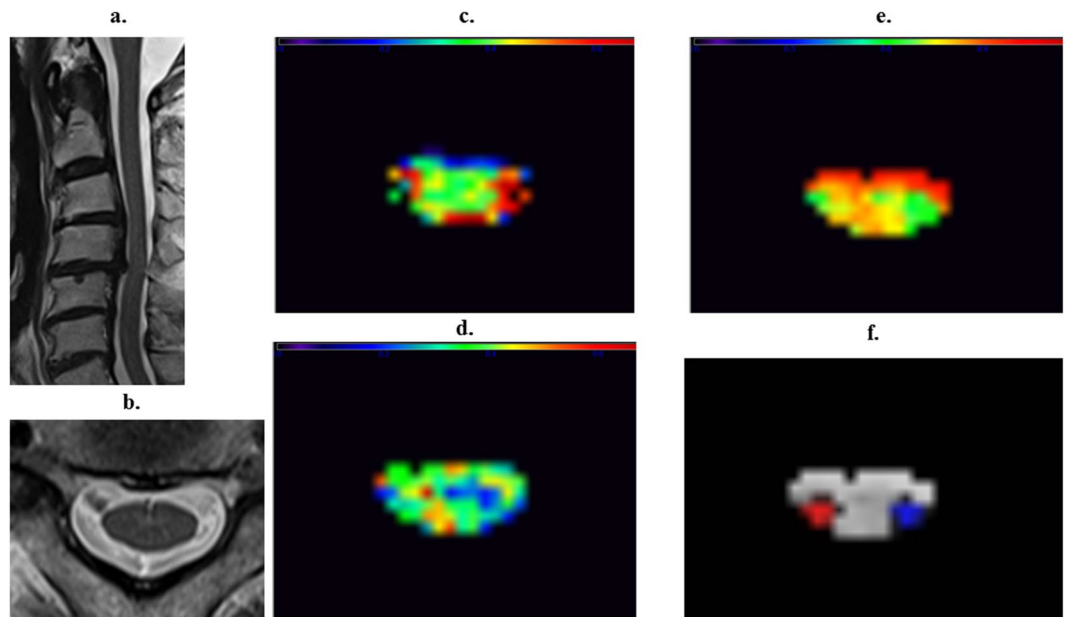


Figure 1. A representative case of cervical spondylotic myelopathy (CSM) (79-year-old male). A sagittal T2-weighted image shows deformation of cervical vertebrae and spinal canal stenosis at C4-5 level (a). A transverse T2-weight image at C3 vertebral level shows no abnormal intensity in the spinal cord (b). Myelin volume fraction map at C3 vertebral level shows no definite laterality (c) but axon volume fraction (d) and g-ratio map (e) show the lower values in the left lateral funiculi. Right (red) and left (blue) lateral corticospinal tract ROIs of PAM50 atlas co-registered to patient's space are projected on g-ratio map (f). Note that liner high values on the edge of the spinal cord may indicate registration error.

axonal loss and degeneration were observed in the lateral funiculi, including the lateral corticospinal tracts, at the early stage of CSM, whereas the posterior columns were damaged at the later stages³⁵. Our AVF results were consistent with these reported pathologic changes. Therefore, measuring the AVF and the g-ratio is an appropriate method to observe the microstructural pathological changes in the spinal cord, which are not demonstrated by conventional MR imaging. Although direct comparison between the disease severity and the MVE, the AVF and the g-ratio was not performed in this study, another study has revealed that MRI shows disease progression more often than clinical measures do, possibly because incremental injury does not necessarily manifest with neurological/functional deficits³⁷. Promoting axonal plasticity may be useful to improve neurological function in CSM³⁸, so estimation of microstructural changes in the spinal cord by MR imaging including the MVE, the AVF and the g-ratio will play an important role for patient management, with development of regenerative medicine.

There are several limitations in the present study. First, several MR imaging and analysis methods have been introduced for AVF and MVE imaging, and a standard MR imaging method remains to be established. Therefore, our results may be changed by using a different method to calculate the AVF and the MVE. For the AVF, the NODDI model derived from 2-shell dMRI was used in this study, but this was a method generally optimized for brain imaging. A more suitable method for estimating AVF may be possible; for example, double-diffusion-encoded measurements is a good candidate³⁹. In addition, even though we used the PAM 50 atlas for localization of each white matter tract, another atlas⁴⁰ may lead to different results.

Another limitation was the small number of patients, and there was no assessment of the correlation between the AVF, the MVE or the g-ratio and patients' prognosis. Moreover, symptom laterality is not a conventionally classified feature for study as this, although more relevant now in the study using tractography⁴¹. Longitudinal studies with a larger cohort investigating correlations between clinical outcome and these metrics are needed in the future.

A third limitation was that there was no direct comparison between the AVF, the MVE or the g-ratio and histology. However, Duval *et al.* reported that using histology as ground truth has some limitations, such as degeneration of tissue specimen during preparation for optical imaging¹⁹. Therefore, at least for clinical use, the correlation between the MR indices and symptoms seems to be more important.

In conclusion, our results show the pathological microstructural changes in the spinal cord in patients with CSM, such as partial axonal degenerations. More studies investigating the correlation between imaging, pathology and clinical assessments are needed. The technique we used has the potential to provide new information and be a *in vivo* clinical biomarker in patients with CSM.

Materials and Methods

Subjects. Twenty-four patients with clinically diagnosed cervical spondylotic myelopathy (CSM) (12 women and 12 men, mean age 61 years) and nearly age matched 5 healthy controls without history of neurological disease from local area were enrolled in this study. The mean Japanese Orthopaedic Association score (JOA score) of the

	Fasciculus gracilis	Fasciculus cuneatus	Lateral corticospinal tracts
AVF			
Affected (n=26)	0.31 ± 0.05*	0.33 ± 0.06*	0.28 ± 0.06*
Unaffected (n=14)	0.31 ± 0.05	0.35 ± 0.07*	0.29 ± 0.06*
Control (n=10)	0.36 ± 0.04*	0.42 ± 0.03*	0.38 ± 0.07*
MVF			
Affected (n=26)	0.31 ± 0.04	0.30 ± 0.03	0.37 ± 0.06
Unaffected (n=14)	0.32 ± 0.05	0.31 ± 0.04	0.36 ± 0.08
Control (n=10)	0.32 ± 0.02	0.30 ± 0.03	0.32 ± 0.08
g-ratio			
Affected (n=26)	0.68 ± 0.05	0.70 ± 0.05	0.65 ± 0.06*
Unaffected (n=14)	0.69 ± 0.04	0.72 ± 0.05	0.66 ± 0.07
Control (n=10)	0.69 ± 0.05	0.74 ± 0.04	0.70 ± 0.03*

Table 2. The values represent mean ± SD, a.u. *P < 0.05. Metrics showing significant differences are connected to each other by lines.

patients was 15.6 ± 1.6 (mean ± SD). Symptoms of all the patients were only mild tingling sensation on either or both hands. By referring to conventional MR imaging, including T2- and T1-weighted images, and electronic medical records, including the laterality of symptoms of the patients, two experienced neuroradiologists (R.I. and M.H.) classified the laterality of the disease into two groups, the affected side and the unaffected side. Specifically, affected side was determined if the side of compression of the spinal cord by osteophyte and/or extruded spinal disk confirmed on conventional MR images matched the side of clinical symptom and electronic medical records. Moreover, if a patient had bilateral symptoms and spinal cord is compressed bilaterally, both right and left sides of the spinal cord were considered to be affected. Exclusion criteria for analysis were as follows: (a) the presence of other spinal disease; (b) a history of neck surgery for any disease. In all patients, level of stenosis was at either one or combination of C4/5, C5/6, and C6/7.

Ethical issues. All data from the patients were obtained in accordance with the 2013 revised Helsinki Declaration of 1964. We provided participants with detailed information, and written informed consent was obtained from all participants. The Ethical Committee of Juntendo University Hospital approved the study.

Data acquisition. After conventional MR imaging, including T2- and T1-weighted imaging, in the sagittal and transverse planes, quantitative MR imaging data of 2-shell dMRI using a prototype sequence based on simultaneous multi-slice (SMS) accelerated readout-segmented echo planar imaging (rs-EPI), which is essentially multi-shot echo-planar DWI for calculating the AVF and MTsat imaging for calculating the MVF, were acquired with a 3 Tesla scanner (MAGNETOM Skyra, Siemens Healthcare, Erlangen, Germany) with a body coil excitation and 64-ch head/neck coil for reception.

Axon imaging. We have chosen NODDI for axon estimation in this study because one of the NODDI-derived quantitative metrics, intracellular volume fraction (Vic), is believed to comprise the signal of axons in the white matter²⁸. Furthermore, NODDI is more robust for estimating the axon volume in the fiber crossing area than the fractional anisotropy of DTI^{15,42}. Thus, NODDI seems to be the best reasonable method available to estimate the AVF in a clinical setting considering its tolerable acquisition time for patients and its reliability. To acquire 2-shell dMRI data for NODDI, rs-EPI sequence was chosen because of its low distortion and relatively high signal-to-noise ratio^{43,44}, and accelerated with SMS⁴⁵, which has been shown to cause low level of distortion while preserving the quality of data in the spine⁴⁶.

The imaging parameters for 2-shell dMRI were as follows: repetition time(TR)/echo time, 3000/104 (ms/ms); echo space, 0.50 ms; number of signals acquired, one; section thickness, 4 mm; number of slices, 39; field of view, 200×200 mm²; matrix, 200×200 ; number of shots, 5; SMS factor, 3; bandwidth, 260 Hz/pixel; parallel imaging using GRAPPA factor 2 in phase-encoding direction; 7/8 partial Fourier acquisition; imaging time, approximately 8 min; 2 b values (1000 and 2000 s/mm²) with a b = 0 image and diffusion encoding in 20 directions for each b value.

Myelin imaging. We have chosen MTsat for myelin estimation in this study because MTsat showed good correlation with qMT⁴², which was thought to be a suitable method for myelin quantification but required a scanning

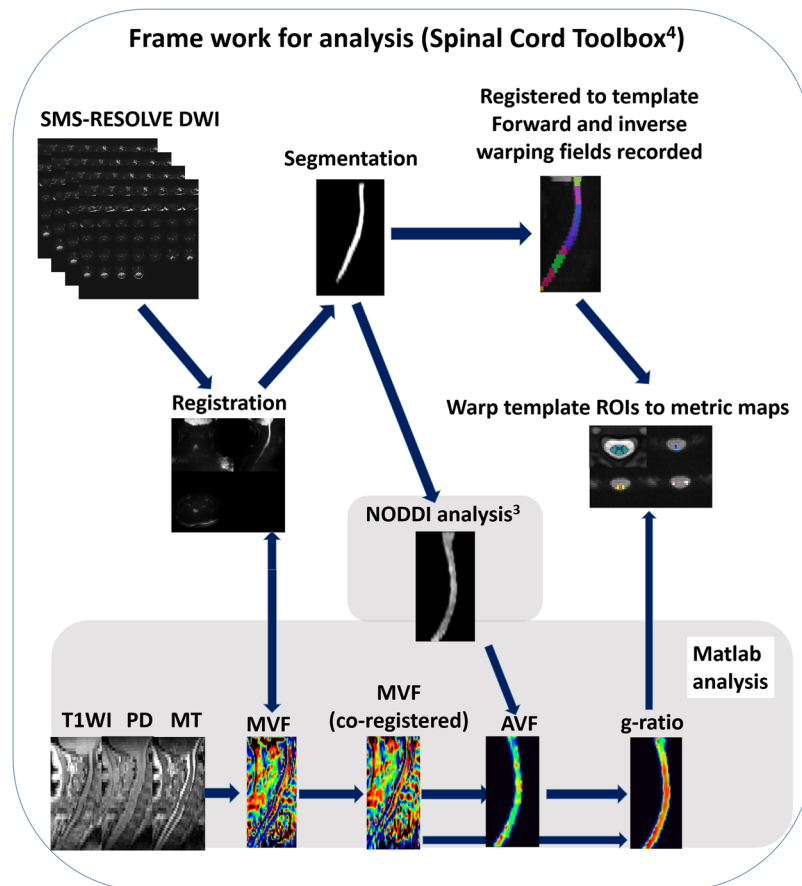


Figure 2. The procedure for generating the myelin volume fraction (MVF), axon volume fraction (AVF) and g-ratio maps. Using the Spinal Cord Toolbox (SCT), diffusion MRI (dMRI) data were registered to each other and segmented in the spinal cord. The spinal cord segmented from magnetization transfer (MT)-weighted image using the SCT was registered to the spinal cord segmented from dMRI data. The MVF map generated from T1-weighted, PD-weighted and MT-weighted images using an in-house MATLAB program was registered to dMRI data using the same warping field. dMRI data of segmented spinal cord were used for NODDI analysis with MATLAB, and the generated ICVF and ISO maps were used for generating the AVF map, followed by the g-ratio map. Segmented spinal cord dMRI data were registered to the PAM 50 template using the SCT, and the template ROI was warped to each subject's data to measure the AVF, the MVF and the g-ratio in each white matter tract.

time that was intolerable to patients. In addition, MTsat seems to be a clinically feasible candidate for g-ratio mapping *in vivo*¹³. Three 3D multi-echo fast low-angle shot (FLASH) sequences were performed with predominant T₁-, PD-, and MT-weighting. The imaging parameters for MTsat were as follows: MT-off and MT-on scanning (TR/TE = 24/2.53 ms, flip angle = 5 degrees) and T₁-weighted imaging (TR/TE = 10/2.53 ms, flip angle = 13 degrees); parallel imaging using GRAPPA factor 2 in phase-encoding direction; 7/8 partial Fourier acquisition in the partition direction; bandwidth, 260 Hz/pixel with the same spatial resolution and slice coverage for 2-shell DWI. Two additional B₁ maps using EPI with short acquisition time (about 10 seconds each) were acquired for correction of B₁ inhomogeneity using the double angle technique⁴⁷ with 10° and 20° flip angles. Imaging time was approximately 7 min total for MTsat.

Post-processing and MR fiber g-ratio calculation. MTsat data were analyzed using an in-house MATLAB script for computing the MVF map, based on a theory in the literature²². First, apparent longitudinal relaxation rate R_{1app} was calculated as following:

$$R_{1app} = \frac{1}{2} \frac{S_{T_1} \alpha_{T_1} / TR_{T_1} - S_{PD} \alpha_{PD} / TR_{PD}}{S_{PD} / \alpha_{PD} - S_{T_1} / \alpha_{T_1}} \quad (1)$$

where S_{T_1} and S_{PD} denote signal intensities of T₁-weighted and PD-weighted images, respectively; TR_{T_1} and TR_{PD} denote TR of T₁-weighted and PD-weighted images, respectively; and α_{T_1} and α_{PD} denote excitation flip angles of T₁-weighted and PD-weighted images, respectively.

Second, apparent signal amplitude A_{app} was calculated as following:

$$A_{\text{app}} = S_{\text{PD}} S_{\text{T1}} \frac{\text{TR}_{\text{PD}} \alpha_{\text{T1}} / \alpha_{\text{PD}} - \text{TR}_{\text{T1}} \alpha_{\text{PD}} / \alpha_{\text{T1}}}{S_{\text{T1}} \text{TR}_{\text{PD}} \alpha_{\text{T1}} - S_{\text{PD}} \text{TR}_{\text{T1}} \alpha_{\text{PD}}} \quad (2)$$

Third, apparent MT saturation δ_{app} was calculated as following:

$$\delta_{\text{app}} = (A_{\text{app}} \alpha_{\text{MT}} / S_{\text{MT}} - 1) R_{1\text{app}} \text{TR}_{\text{MT}} - \alpha_{\text{MT}}^2 / 2 \quad (3)$$

where S_{MT} , TR_{MT} , and α_{MT} denote signal intensity, TR, and excitation flip angle of MT-weighted image, respectively.

To use δ_{app} as an absolute quantitative marker of myelin, we assumed linear proportional relationship between δ_{app} and MVF⁴². Calibration factor was determined for g-ratio in the corpus callosum to be around 0.7, as suggested by Mohammadi *et al.*¹³. Scanning for this calibration was performed in another cohort of 3 subjects with similar protocol to that used in the current study.

For the AVF, neurite orientation dispersion and density imaging (NODDI)²⁸ model analysis was employed using dMRI data for Vic, and isotropic water diffusion volume fraction (Viso) indicating free water was calculated using the NODDI MATLAB toolbox (available at https://www.nitrc.org/projects/noddi_toolbox). Then, the AVF was estimated by the following equation: $\text{AVF} = (1 - \text{MVF})(1 - \text{Viso})\text{Vic}$ ¹⁵. The aggregate MR fiber g-ratio was calculated as a function of the MVF and the AVF: $\text{g-ratio} = \sqrt{(\text{AVF} / (\text{MVF} + \text{AVF}))}$. Additionally, semi-automated analysis was performed using the Spinal Cord Toolbox³¹ for segmentation, motion correction, registration to the WM atlas (PAM50 template), co-registration between the MVF and the AVF maps and extraction of metrics. These imaging procedures are summarized in Fig. 2.

In each of the affected and unaffected sides of patients' spinal cords and spinal cords of healthy volunteers, quantitative metrics in three relatively large white matter tracts in the cervical spinal cord dorsal columns (DCs) at the C3 vertebral level, including the fasciculus gracilis, fasciculus cuneatus, and lateral corticospinal tracts (LCSTs), were selected and compared. To avoid the compressed area of the spinal cord, which could yield biased and incorrect measurements, the C3 vertebral level, which was above the level of stenosis, was selected for ROI analysis⁴⁸.

Moreover, we evaluated among mJOA scores, number of levels of compression and the above quantitative MR metrics.

Statistical evaluations were performed with IBM SPSS Statistics software (version 19.0; SPSS, Chicago, IL), using one-way ANOVA with Scheffé's post hoc test between the values from affected and unaffected sides of spinal cords in patients and spinal cords in healthy controls. A p-value less than 0.05 was considered to indicate a statistically significant difference.

The datasets generated during and analyzed during the current study are available from the corresponding author on reasonable request.

References

- Young, W. F. Cervical spondylotic myelopathy: a common cause of spinal cord dysfunction in older persons. *Am Fam Physician* **62**(1064–1070), 1073 (2000).
- Yu, W. R., Liu, T., Kiehl, T. R. & Fehlings, M. G. Human neuropathological and animal model evidence supporting a role for Fas-mediated apoptosis and inflammation in cervical spondylotic myelopathy. *Brain* **134**, 1277–1292, <https://doi.org/10.1093/brain/awr054> (2011).
- Moon, E. S., Karadimas, S. K., Yu, W. R., Austin, J. W. & Fehlings, M. G. Riluzole attenuates neuropathic pain and enhances functional recovery in a rodent model of cervical spondylotic myelopathy. *Neurobiol Dis* **62**, 394–406, <https://doi.org/10.1016/j.nbd.2013.10.020> (2014).
- Cohen-Adad, J. *et al.* Demyelination and degeneration in the injured human spinal cord detected with diffusion and magnetization transfer MRI. *Neuroimage* **55**, 1024–1033, <https://doi.org/10.1016/j.neuroimage.2010.11.089> (2011).
- Demir, A. *et al.* Diffusion-weighted MR imaging with apparent diffusion coefficient and apparent diffusion tensor maps in cervical spondylotic myelopathy. *Radiology* **229**, 37–43, <https://doi.org/10.1148/radiol.2291020658> (2003).
- Hori, M. *et al.* New diffusion metrics for spondylotic myelopathy at an early clinical stage. *Eur Radiol* **22**, 1797–1802, <https://doi.org/10.1007/s00330-012-2410-9> (2012).
- Mamata, H., Jolesz, F. A. & Maier, S. E. Apparent diffusion coefficient and fractional anisotropy in spinal cord: age and cervical spondylosis-related changes. *J Magn Reson Imaging* **22**, 38–43, <https://doi.org/10.1002/jmri.20357> (2005).
- Holly, L. T., Freitas, B., McArthur, D. L. & Salamon, N. Proton magnetic resonance spectroscopy to evaluate spinal cord axonal injury in cervical spondylotic myelopathy. *J Neurosurg Spine* **10**, 194–200, <https://doi.org/10.3171/2008.12.SPINE08367> (2009).
- Ellingson, B. M., Salamon, N., Hardy, A. J. & Holly, L. T. Prediction of Neurological Impairment in Cervical Spondylotic Myelopathy using a Combination of Diffusion MRI and Proton MR Spectroscopy. *PLoS One* **10**, e0139451, <https://doi.org/10.1371/journal.pone.0139451> (2015).
- Martin, A. R. *et al.* Translating state-of-the-art spinal cord MRI techniques to clinical use: A systematic review of clinical studies utilizing DTI, MT, MWF, MRS, and fMRI. *Neuroimage Clin* **10**, 192–238, <https://doi.org/10.1016/j.nicl.2015.11.019> (2016).
- Ellingson, B. M., Salamon, N., Woodworth, D. C. & Holly, L. T. Correlation between degree of subvoxel spinal cord compression measured with super-resolution tract density imaging and neurological impairment in cervical spondylotic myelopathy. *J Neurosurg Spine* **22**, 631–638, <https://doi.org/10.3171/2014.10.SPINE14222> (2015).
- Grabher, P. *et al.* Voxel-based analysis of grey and white matter degeneration in cervical spondylotic myelopathy. *Sci Rep* **6**, 24636, <https://doi.org/10.1038/srep24636> (2016).
- Mohammadi, S. *et al.* Whole-Brain *In-vivo* Measurements of the Axonal G-Ratio in a Group of 37 Healthy Volunteers. *Front Neurosci* **9**, 441, <https://doi.org/10.3389/fnins.2015.00441> (2015).
- Stikov, N. *et al.* Quantitative analysis of the myelin g-ratio from electron microscopy images of the macaque corpus callosum. *Data Brief* **4**, 368–373, <https://doi.org/10.1016/j.dib.2015.05.019> (2015).
- Stikov, N. *et al.* *In vivo* histology of the myelin g-ratio with magnetic resonance imaging. *Neuroimage* **118**, 397–405, <https://doi.org/10.1016/j.neuroimage.2015.05.023> (2015).
- Hagiwara, A. *et al.* Analysis of White Matter Damage in Patients with Multiple Sclerosis via a Novel *In Vivo* MR Method for Measuring Myelin, Axons, and G-Ratio. *AJNR Am J Neuroradiol* **38**, 1934–1940, <https://doi.org/10.3174/ajnr.A5312> (2017).

17. Cercignani, M. *et al.* Characterizing axonal myelination within the healthy population: a tract-by-tract mapping of effects of age and gender on the fiber g-ratio. *Neurobiol Aging* **49**, 109–118, <https://doi.org/10.1016/j.neurobiolaging.2016.09.016> (2017).
18. Dean, D. C. 3rd *et al.* Mapping an index of the myelin g-ratio in infants using magnetic resonance imaging. *Neuroimage* **132**, 225–237, <https://doi.org/10.1016/j.neuroimage.2016.02.040> (2016).
19. Duval, T. *et al.* g-Ratio weighted imaging of the human spinal cord *in vivo*. *Neuroimage* **145**, 11–23, <https://doi.org/10.1016/j.neuroimage.2016.09.018> (2017).
20. Mezer, A. *et al.* Quantifying the local tissue volume and composition in individual brains with magnetic resonance imaging. *Nat Med* **19**, 1667–1672, <https://doi.org/10.1038/nm.3390> (2013).
21. Sled, J. G. & Pike, G. B. Quantitative interpretation of magnetization transfer in spoiled gradient echo MRI sequences. *J Magn Reson* **145**, 24–36, <https://doi.org/10.1006/jmre.2000.2059> (2000).
22. Helms, G., Dathe, H., Kallenberg, K. & Dechent, P. High-resolution maps of magnetization transfer with inherent correction for RF inhomogeneity and T1 relaxation obtained from 3D FLASH MRI. *Magn Reson Med* **60**, 1396–1407, <https://doi.org/10.1002/mrm.21732> (2008).
23. Ganzetti, M., Wenderoth, N. & Mantini, D. Whole brain myelin mapping using T1- and T2-weighted MR imaging data. *Front Hum Neurosci* **8**, 671, <https://doi.org/10.3389/fnhum.2014.00671> (2014).
24. Hagiwara, A. *et al.* SyMRI of the Brain: Rapid Quantification of Relaxation Rates and Proton Density, With Synthetic MRI, Automatic Brain Segmentation, and Myelin Measurement. *Invest Radiol* **52**, 647–657, <https://doi.org/10.1097/RLI.0000000000000365> (2017).
25. Basser, P. J. & Pierpaoli, C. Microstructural and physiological features of tissues elucidated by quantitative-diffusion-tensor MRI. *J Magn Reson B* **111**, 209–219 (1996).
26. Assaf, Y., Mayk, A. & Cohen, Y. Displacement imaging of spinal cord using q-space diffusion-weighted MRI. *Magn Reson Med* **44**, 713–722, [https://doi.org/10.1002/1522-2594\(200011\)44:5<713::AID-MRM9>3.0.CO;2-6](https://doi.org/10.1002/1522-2594(200011)44:5<713::AID-MRM9>3.0.CO;2-6) (2000).
27. Hori, M. *et al.* Visualizing non-Gaussian diffusion: clinical application of q-space imaging and diffusional kurtosis imaging of the brain and spine. *Magn Reson Med Sci* **11**, 221–233 (2012).
28. Zhang, H., Schneider, T., Wheeler-Kingshott, C. A. & Alexander, D. C. NODDI: practical *in vivo* neurite orientation dispersion and density imaging of the human brain. *Neuroimage* **61**, 1000–1016, <https://doi.org/10.1016/j.neuroimage.2012.03.072> (2012).
29. Grussu, F., Schneider, T., Zhang, H., Alexander, D. C. & Wheeler-Kingshott, C. A. Neurite orientation dispersion and density imaging of the healthy cervical spinal cord *in vivo*. *Neuroimage* **111**, 590–601, <https://doi.org/10.1016/j.neuroimage.2015.01.045> (2015).
30. Okita, G. *et al.* Application of neurite orientation dispersion and density imaging or diffusion tensor imaging to quantify the severity of cervical spondylotic myelopathy and to assess postoperative neurologic recovery. *Spine J.* <https://doi.org/10.1016/j.spinee.2017.07.007> (2017).
31. De Leener, B. *et al.* SCT: Spinal Cord Toolbox, an open-source software for processing spinal cord MRI data. *Neuroimage* **145**, 24–43, <https://doi.org/10.1016/j.neuroimage.2016.10.009> (2017).
32. Peterson, D. J. *et al.* Test-Retest and Interreader Reproducibility of Semiautomated Atlas-Based Analysis of Diffusion Tensor Imaging Data in Acute Cervical Spine Trauma in Adult Patients. *AJNR Am J Neuroradiol* **38**, 2015–2020, <https://doi.org/10.3174/ajnr.A5334> (2017).
33. Martin, A. R. *et al.* Clinically Feasible Microstructural MRI to Quantify Cervical Spinal Cord Tissue Injury Using DTI, MT, and T2*-Weighted Imaging: Assessment of Normative Data and Reliability. *AJNR Am J Neuroradiol* **38**, 1257–1265, <https://doi.org/10.3174/ajnr.A5163> (2017).
34. McCoy, D. B. *et al.* MRI Atlas-Based Measurement of Spinal Cord Injury Predicts Outcome in Acute Flaccid Myelitis. *AJNR Am J Neuroradiol* **38**, 410–417, <https://doi.org/10.3174/ajnr.A5044> (2017).
35. Ito, T., Oyanagi, K., Takahashi, H., Takahashi, H. E. & Ikuta, F. Cervical spondylotic myelopathy. Clinicopathologic study on the progression pattern and thin myelinated fibers of the lesions of seven patients examined during complete autopsy. *Spine (Phila Pa 1976)* **21**, 827–833 (1996).
36. Kim, P., Haisa, T., Kawamoto, T., Kirino, T. & Wakai, S. Delayed myelopathy induced by chronic compression in the rat spinal cord. *Ann Neurol* **55**, 503–511, <https://doi.org/10.1002/ana.20018> (2004).
37. Martin, A. R. *et al.* Toward Clinical Translation of Quantitative Spinal Cord MRI: Serial Monitoring to Identify Disease Progression in Patients with Degenerative Cervical Myelopathy. In Proceedings of the 25th Annual Meeting of International Society for Magnetic Resonance in Medicine, Honolulu, HI, USA 2509 (ISMRM, 2017).
38. Dhillon, R. S. *et al.* Axonal plasticity underpins the functional recovery following surgical decompression in a rat model of cervical spondylotic myelopathy. *Acta Neuropathol Commun* **4**, 89, <https://doi.org/10.1186/s40478-016-0359-7> (2016).
39. Skinner, N. P., Kurpad, S. N., Schmit, B. D., Tugan Muftuler, L. & Budde, M. D. Rapid *in vivo* detection of rat spinal cord injury with double-diffusion-encoded magnetic resonance spectroscopy. *Magn Reson Med* **77**, 1639–1649, <https://doi.org/10.1002/mrm.26243> (2017).
40. Taso, M. *et al.* A reliable spatially normalized template of the human spinal cord—Applications to automated white matter/gray matter segmentation and tensor-based morphometry (TBM) mapping of gray matter alterations occurring with age. *Neuroimage* **117**, 20–28, <https://doi.org/10.1016/j.neuroimage.2015.05.034> (2015).
41. Maki, S. *et al.* Tract-Specific Diffusion Tensor Imaging Reveals Laterality of Neurological Symptoms in Patients with Cervical Compression Myelopathy. *World Neurosurg* **96**, 184–190, <https://doi.org/10.1016/j.wneu.2016.08.129> (2016).
42. Campbell, J. S. W. *et al.* Promise and pitfalls of g-ratio estimation with MRI. *Neuroimage.* <https://doi.org/10.1016/j.neuroimage.2017.08.038> (2017).
43. Yamaguchi, K. *et al.* Diagnostic Performance of Diffusion Tensor Imaging with Readout-segmented Echo-planar Imaging for Invasive Breast Cancer: Correlation of ADC and FA with Pathological Prognostic Markers. *Magn Reson Med Sci* **16**, 245–252, <https://doi.org/10.2463/mrms.mp.2016-0037> (2017).
44. Porter, D. A. & Heidemann, R. M. High resolution diffusion-weighted imaging using readout-segmented echo-planar imaging, parallel imaging and a two-dimensional navigator-based reacquisition. *Magn Reson Med* **62**, 468–475, <https://doi.org/10.1002/mrm.22024> (2009).
45. Takamura, T. *et al.* Slice-Accelerated Gradient-Echo Echo Planar Imaging Dynamic Susceptibility Contrast-Enhanced MRI with Blipped CAIPI: Effect of Increasing Temporal Resolution. *Jpn J Radiol* **2017** **36**, 40–50, <https://doi.org/10.1007/s11604-017-0695-y> (2018).
46. Liu, W. *et al.* Large-FOV Tractography of the Brain and Spinal Cord with Reduced Scan Time: A Study using Diffusion-Weighted, Readout-Segmented EPI and Simultaneous Multi-Slice Acceleration. In Proceedings of the 23rd Annual Meeting of International Society for Magnetic Resonance in Medicine, Toronto, Ontario, Canada 4434 (ISMRM, 2015).
47. Morrell, G. R. & Schabel, M. C. An analysis of the accuracy of magnetic resonance flip angle measurement methods. *Phys Med Biol* **55**, 6157–6174, <https://doi.org/10.1088/0031-9155/55/20/008> (2010).
48. Martin, A. R. *et al.* A Prospective Longitudinal Study in Degenerative Cervical Myelopathy Using Quantitative Microstructural MRI with Tract-Specific Metrics. In Proceedings of the 24th Annual Meeting of International Society for Magnetic Resonance in Medicine, Singapore, 853 (ISMRM, 2016).

Acknowledgements

We greatly appreciate Dr. Nikola Stikov for kind advice and help. This work was supported by JSPS KAKENHI Grant Numbers 16K10328 and JP16H06280, Grant-in-Aid for Scientific Research on Innovative Areas - Resource and technical support platforms for promoting research of 'Advanced Bioimaging Support' and the ImPACT Program of the Council for Science, Technology and Innovation (Cabinet Office, Government of Japan).

Author Contributions

M.H., K.K., Y.S., W.L., K.M., K.K., K.K.K., M.S. and S.A. conceived the study. M.H. and H.A. wrote the main manuscript text. I.F. and N.H. conducted experiments. M.H., R.U., I.F., T.T., and R.I. analyzed results. All authors reviewed the manuscript.

Additional Information

Competing Interests: The authors declare no competing interests.

Publisher's note: Springer Nature remains neutral with regard to jurisdictional claims in published maps and institutional affiliations.



Open Access This article is licensed under a Creative Commons Attribution 4.0 International License, which permits use, sharing, adaptation, distribution and reproduction in any medium or format, as long as you give appropriate credit to the original author(s) and the source, provide a link to the Creative Commons license, and indicate if changes were made. The images or other third party material in this article are included in the article's Creative Commons license, unless indicated otherwise in a credit line to the material. If material is not included in the article's Creative Commons license and your intended use is not permitted by statutory regulation or exceeds the permitted use, you will need to obtain permission directly from the copyright holder. To view a copy of this license, visit <http://creativecommons.org/licenses/by/4.0/>.

© The Author(s) 2018